Photoproduction of η and η' mesons off protons

V. Crede,[1] A. McVeigh,[1] A. V. Anisovich,[2,3] J. C. S. Bacelar,[4] R. Bantes,[2] O. Bartholomy,[2] D. Bayadilov,[2,3] R. Beck,[2] Y. A. Beloglazov,[3] R. Castelijns,[4] A. Ehmanns,[2] D. Elsner,[5] K. Essig,[2] R. Ewald,[5] I. Fabry,[2] M. Fuchs,[2] Chr. Funke,[2] R. Gothe,[5] R. Gregor,[6] A. Gridnev,[3] E. Gutz,[2] St. Höffgen,[5] P. Hoffmeister,[2] I. Horn,[2] I. Jaegle,[7] J. Junkersfeld,[2] H. Kalinowsky,[2] S. Kammer,[5] Frank Klein,[5] Friedrich Klein,[5] E. Klempt,[2] M. Konrad,[5] M. Kotulla,[6,7] B. Krusche,[7] J. Langheinrich,[5] H. Löhner,[4] I. V. Lopatin,[3] J. Lotz,[2] S. Lugert,[6] D. Menze,[5] T. Mertens,[7] J. G. Messchendorp,[4,6] V. Metag,[6] M. Nanova,[6] V. A. Nikonov,[2,3] D. Novinski,[3] R. Novotny,[6] M. Ostrick,[5] L. M. Pant,[6] H. van Pee,[2] M. Pfeiffer,[6] A. Roy,[6] A. V. Sarantsev,[2,3] S. Schadmand,[8] C. Schmidt,[2] H. Schmieden,[5] B. Schoch,[5] S. Shende,[4] V. Sokhoyan,[2] N. Sparks,[1] A. Süle,[5] V. V. Sumachev,[3] T. Szczepanek,[2] U. Thoma,[2] D. Trnka,[6] R. Varma,[6] D. Walther,[2,5] Ch. Weinheimer,[2] Ch. Wendel,[2] and A. Wilson[1]
(CBELSA/TAPS Collaboration)

[1]*Department of Physics, Florida State University, Tallahassee, Florida 32306, USA*
[2]*Helmholtz-Institut für Strahlen- und Kernphysik der Universität Bonn, D-53115 Bonn, Germany*
[3]*Petersburg Nuclear Physics Institute, RU-188350 Gatchina, Russia*
[4]*KVI, 9747 AA Groningen, The Netherlands*
[5]*Physikalisches Institut, Universität Bonn, D-53115 Bonn, Germany*
[6]*II. Physikalisches Institut, Universität Gießen, D-35392 Gießen, Germany*
[7]*Physikalisches Institut, Universität Basel, CH-4056 Basel, Switzerland*
[8]*Institut für Kernphysik, Forschungszentrum Jülich, D-52428 Jülich, Germany*

(Received 8 September 2009; published 6 November 2009)

Total and differential cross sections for η and η'photoproduction off the proton have been determined with the CBELSA/TAPS detector for photon energies between 0.85 and 2.55 GeV. The η mesons are detected in their two neutral decay modes, $\eta \to \gamma\gamma$ and $\eta \to 3\pi^0 \to 6\gamma$, and for the first time, cover the full angular range in $\cos\theta_{c.m.}$ of the η meson. These new η photoproduction data are consistent with the earlier CB-ELSA results. The η' mesons are observed in their neutral decay to $\pi^0\pi^0\eta \to 6\gamma$ and also extend the coverage in angular range.

DOI: 10.1103/PhysRevC.80.055202 PACS number(s): 25.20.Lj, 13.25.−k, 13.60.Le, 13.75.Gx

I. INTRODUCTION

Understanding the structure of the proton and its excited states is one of the key questions in hadronic physics. Known as the missing-baryon problem, quark models based on three constituent quark degrees of freedom predict many more states than have been observed experimentally. Baryon resonances are broad and widely overlap, especially at higher energies, imposing challenges on the interpretation of experimental data in terms of resonance contributions. Without precise data from many decay channels, it will be difficult or even impossible to accurately determine the properties of well-established resonances, or to confirm or rule out the existence of weakly established resonances or new, so far unobserved, states.

Of particular importance are well-chosen decay channels that can help isolate contributions from individual excited states and clarify their importance. Photoproduction of η and η' mesons offers the distinct advantage of serving as an isospin filter for the spectrum of nucleon resonances and, thus, simplifies data interpretations and theoretical efforts to predict the excited states contributing to these reactions. Because the η and η' mesons have isospin $I = 0$, the $N\eta$ and $N\eta'$ final states can only originate from intermediate $I = 1/2$ nucleon states.

Data on η photoproduction off the free proton were obtained and studied at many different laboratories over a wide kinematic range [1–11]. A review of the main data sets and a corresponding comparison of their coverage in energy and solid angle can be found in Ref. [12]. Almost all analyses found that the $N(1535)S_{11}$ nucleon resonance dominates η photoproduction at threshold, although there are models that do not need the $N(1535)S_{11}$ resonance to describe the threshold production of η mesons [13]. The $N(1535)S_{11}$ state is well known for its large $N\eta$ coupling, whereas other resonances couple only weakly to $N\eta$. Small contributions from the $N(1520)D_{13}$ resonance via interference with the S_{11} resonance have been determined from data on photon beam asymmetries [2,9] and angular distributions. Data from target polarization experiments [3] revealed surprising effects concerning the phase relations of the s- and d-wave amplitudes [14]. Despite its four-star assignment by the Particle Data Group (PDG) [15], the role and nature of the $N(1535)S_{11}$ is still not well understood. Surprisingly, the $N(1650)S_{11}$ nucleon resonance has the same quantum numbers, but shows no strong $N\eta$ coupling. Many different arguments have been discussed to explain this observation; the two S_{11} states can have appreciable mixing [16], for instance. The $N(1535)S_{11}$ resonance can also be a dynamically generated state of the $\Sigma K - p\eta$ system [17] or, more generally, a dynamically generated resonance coming from the interaction of the octet of pseudoscalar mesons with the ground-state octet of baryons [18,19]. Recent efforts at Jefferson Laboratory have concentrated on describing the $\gamma p \to N^*$ transitions by the interaction of the photon with the three-quark core of the resonance including meson-cloud effects in the low Q^2 region [20]. The agreement of the model predictions for the helicity

amplitude $A_{1/2}$ with experimental data ranges from good for some lower-lying $N^\star$ states to fair for the $N(1535)S_{11}$, not ruling out alternative explanations.

The importance of contributions from the $N(1650)S_{11}$ resonance to η photoproduction has been discussed further in conjunction with its photoproduction off the neutron. Recently, the neutron data have attracted interest because of the observation of a bump-like structure at 1.67 GeV/c^2 [21,22], which has not been seen in the cross section off the proton. In Ref. [23], it has been shown that a strong interference between $S_{11}(1535)$, $S_{11}(1650)$, and a nonresonant background can provide a good description of these data.

A partial wave analysis (PWA) of recent CB-ELSA data in the framework of the Bonn-Gatchina (BnGa) model [24], which included data on other reactions and from other experiments, found the dominance of three nucleon resonances in η photoproduction: $N(1535)S_{11}$, $N(1720)P_{13}$, and a proposed new state, $N(2070)D_{15}$ [8]. The large $N\eta$ coupling of the $N(1720)P_{13}$ was surprising. Solutions of the η-MAID model [25] in this mass range assign much of the intensity to the $N(1710)P_{11}$ instead. Current efforts with regard to the extraction of double-polarization observables will help shed light on this controversy. The data presented here cover the full angular range and, within the framework of the Bonn-Gatchina model, are still consistent with the dominance of the three nucleon resonances, $N(1535)S_{11}$, $N(1720)P_{13}$, and $N(2070)D_{15}$.

Data on η' photoproduction are scarce. Analyses published before 2005 observed fewer than 300 η' events [26–28], and an interpretation in terms of resonance contributions was difficult. Data from Jefferson Laboratory significantly improved the world database [29]. Researchers observed 2×10^5 η' events, which allowed the extraction of differential cross sections. Although more precise than previous measurements, the CLAS data are still limited in their angular coverage. In the model by Nakayama and Haberzettl (Ref. [29] and Ref. [12] therein), the $N\eta'$ final state couples to $N(1535)S_{11}$ and $N(1710)P_{11}$. The authors claim the importance of $J = 3/2$ states ($N(1940)P_{13}$, $N(1780)D_{13}$, $N(2090)D_{13}$) in the process, which are useful to obtain the correct shape of the differential cross sections for energies from 1.728 to 1.879 GeV.

In this article, we present total and differential cross sections for the reactions:

$$\gamma p \to p\eta, \quad \text{where } \eta \to 2\gamma, \tag{1}$$

$$\gamma p \to p\eta, \quad \text{where } \eta \to 3\pi^0 \to 6\gamma, \quad \text{and} \tag{2}$$

$$\gamma p \to p\eta', \quad \text{where } \eta' \to 2\pi^0\eta \to 6\gamma. \tag{3}$$

The data cover an incoming photon energy range up to 2.55 GeV and show the full angular coverage.

The article has the following structure. Section II gives a brief introduction to the CBELSA/TAPS experimental setup. The data reconstruction and selection is discussed in Sec. III, and the extraction of differential and total cross sections is described in Sec. IV. Experimental results are finally presented in Sec. V.

II. EXPERIMENTAL SETUP

The experiment was carried out at the electron accelerator facility ELSA [30] at the University of Bonn using a combination of the Crystal-Barrel (CB) [31] and TAPS [32,33] detectors. The experimental setup is shown in Fig. 1.

Electrons with an energy of 3.175 GeV were extracted from ELSA via slow (resonant) extraction. The bremsstrahlung-tagger photon-beam facility at ELSA delivered unpolarized tagged-photon beams in the energy range from 0.5 to 2.9 GeV by passing the electron beam through a thin copper radiator with a thickness of $(3/1000) \cdot X_R$ (radiation length). Electrons are deflected in the field of the tagger dipole magnet according to their energy loss in the bremsstrahlung process; the remaining energy is determined in a tagger detector consisting of 480 scintillating fibers above 14 scintillation counters (tagger bars) in a configuration with adjacent paddles partially overlapping. The corresponding energy of an emitted photon is $E_\gamma = E_0 - E_{e^-}$. Electrons not undergoing bremsstrahlung are deflected at small angles and guided into a beam dump located behind the tagger detectors. The energy resolution is about 2 MeV for the high-energy photons and 25 MeV for the low-energy part of the bremsstrahlung spectrum.

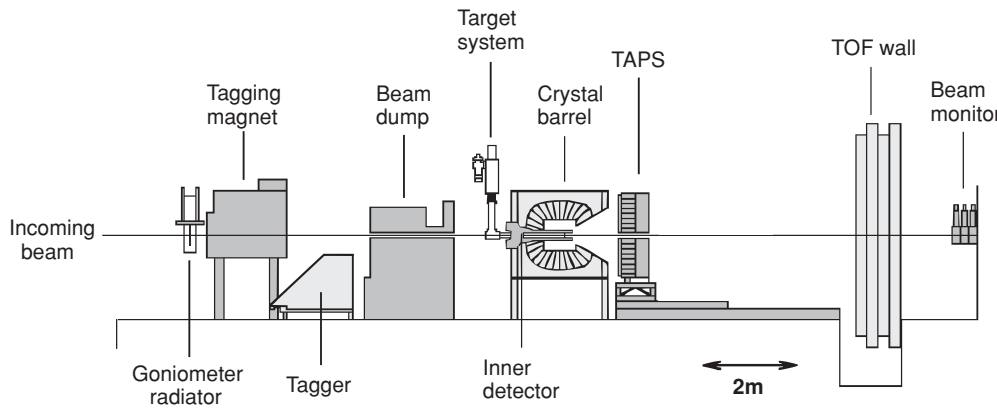

FIG. 1. Experimental setup of CBELSA/TAPS in Bonn. The electron beam delivered by the accelerator ELSA enters from the left side.

For the energy calibration of the tagger, a polynomial was determined in simulations using the measured field map of the bending magnet and the known positions of the fibers. The calibration was cross-checked by measurements with the ELSA electron beam at two different energies. At 600 and 800 MeV, a low-current beam was guided directly into the tagger, while the magnetic field was slowly varied. These results provided corrections to the initial polynomial [34].

The photons hit the liquid hydrogen target in the center of the Crystal-Barrel calorimeter. The target cell (5 cm in length, 3 cm in diameter) was surrounded by a scintillating-fiber detector [35], which provided an unambiguous impact point for charged particles (from the arrangement of its three layers) leaving the target. The CB calorimeter in its CBELSA/TAPS configuration of 2002/2003 consisted of 1290 CsI(Tl) crystals with a length of 16 X_R. The modules have an excellent photon detection efficiency; a detailed description can be found in Ref. [31]. For this series of experiments, the (downstream) rings 11–13 were removed to combine the detector with TAPS in the forward direction. The CB calorimeter covered the complete azimuthal angle and polar angles from 30° to 168°. All crystals are of trapezoidal shape pointing to the center of the target (Fig. 2, top). The TAPS detector consisted of 528 hexagonal BaF_2 crystals with a length of about 12 X_R. It was configured as an hexagonal wall serving as the forward end cap of the CB calorimeter (Fig. 2, bottom). TAPS provided a high granularity in the forward direction covering polar angles between 5° and 30° (full ϕ coverage). A 5-mm-thick plastic scintillator in front of each TAPS module allowed the identification of charged particles. The combination of the Crystal-Barrel and TAPS calorimeters covered 99% of the 4π solid angle and served as an excellent setup to detect multiphoton final states.

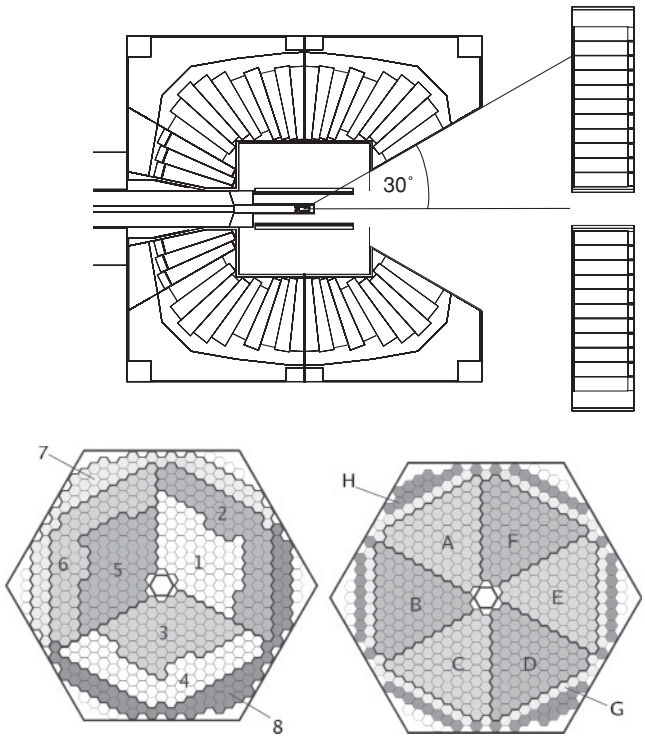

FIG. 2. (Top) Schematic drawing of the liquid hydrogen target, scintillating-fiber detector, and Crystal-Barrel and TAPS calorimeters. (Bottom) Front view of TAPS. The left side shows the logical segmentation for the LED-low trigger; the right side shows the logical segmentation for the LED-high trigger (see text for more details).

The fast response of the TAPS modules provided the first-level trigger. The second-level trigger was based on a cellular logic, fast cluster encoder (FACE), which determined the number of clusters in the barrel. The trigger required either two hits above a low-energy threshold in TAPS [leading-edge discriminator (LED) low] or one hit above a higher-energy threshold in TAPS (LED high) in combination with at least one FACE cluster. The values for the lower-energy thresholds range from 70–80 MeV to 120–170 MeV for TAPS rings closer to the beam line. The higher-energy thresholds are typically 100 MeV higher. The shape of the logical segmentation for the TAPS trigger is shown in Fig. 2 (bottom).

The beam monitor placed at the end of the beam line provided valuable information on the beam intensity (photons not interacting in the H_2 target) used for the determination of the photon flux. This total absorption Čerenkov counter consisted of an array of nine lead glass crystals.

III. DATA ANALYSIS

Data presented here were accumulated from October 2002 until November 2002 in two run periods with ELSA beam energies of 3.175 GeV. For this analysis, only the tagged-photon range up to 2.55 GeV was used, which was covered by the scintillating fibers of the tagger. Higher photon energies can be reconstructed using a wire chamber, which does not provide timing information. The data were used to extract differential and total cross sections for a variety of final states [36,37]. The event reconstruction and selection of the two η photoproduction channels (1) and (2) as well as the η' photoproduction channel, reaction (3), with incident photon energies up to 2.55 GeV are presented in this section. The total number of $\sim 5.5 \times 10^5$ η events was observed ($\sim$422 300 for $\eta \to \gamma\gamma$ and $\sim$126 300 for $\eta \to 3\pi^0$) covering invariant masses from 1510 to 2380 MeV/c^2. For the η' channel, $\sim 5.1 \times 10^3$ events were observed covering invariant masses from 1920 to 2380 MeV/c^2. The η' threshold region, $M \in [1896, 1920]$ MeV/c^2, was analyzed separately using a finer energy binning to better study the threshold behavior.

A. Event reconstruction

Events with at most one proton and with two or six photons were selected, respectively. The charged clusters were identified in TAPS by using the plastic scintillators mounted in front of each BaF_2 crystal. The efficiencies of these (photon)-veto detectors were determined from the data and modeled in the Monte Carlo (MC) program. Typically, the efficiencies have values of about 90%. In the Crystal-Barrel reconstruction, a cluster is assigned to a charged particle if the trajectory from the target center to the barrel hit forms an angle of less than 20° with a trajectory from the target center to a

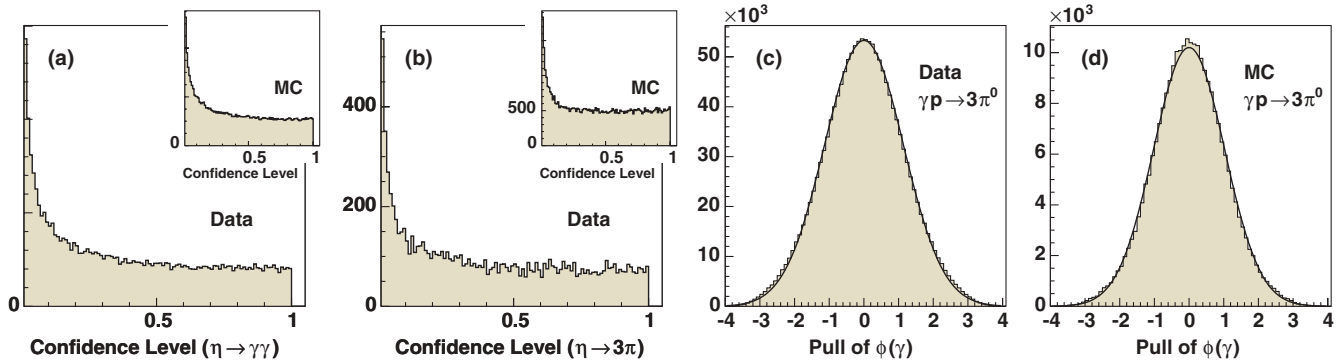

FIG. 3. (Color online) Distributions of confidence levels resulting from a 1C kinematic fit of a true data event sample with two photons in the final state to the hypothesis $\gamma p \to p\gamma\gamma$ (a) and a 4C fit of a six-photon event sample to the hypothesis $\gamma p \to p3\pi^0$ (b) for $E_\gamma \in [1600, 1650]$ MeV. The insets show the same for Monte Carlo data. The strong rise near zero is from poorly reconstructed signal events. Examples of pull distributions for the azimuthal angle ϕ of the final-state photons are shown for data (c) and for Monte Carlo events (d) for the kinematic fit to $\gamma p \to p3\pi^0$ integrated over the full kinematic range. The mean and σ values are 0.0036 and 0.00078 as well as $\sigma = 1.14$ and 1.03, respectively.

hit in the scintillating fiber detector. Proton identification is only used to remove it from the list of photon candidates. The proton momentum is then reconstructed from event kinematics in "missing-proton" kinematic fitting. Proton clusters are on average much smaller than photon clusters and provide worse angular resolution. The proton momentum direction reconstructed from kinematic fitting had to be consistent again with a calorimeter hit when a charged cluster was identified; an angle of less than 15° was required. Our Monte Carlo studies of reaction (1) show that if a proton was observed in the event, the overall misidentification probability is less than 3%.

A kinematic fitter slightly adjusts the measured values within the estimated errors by a minimization procedure until they fulfill exactly certain constraints expressed in the form of equations, which are based on physical conditions such as energy and momentum conservation or invariant masses. The χ^2 probability or confidence level (CL), which is derived from the χ^2 value of the fit, can be used to make judgements and decisions about the goodness of the fit and provides an ideal method to judge possible final-state hypotheses for an event. For Gaussian-distributed errors of the measured particle properties, confidence levels should be flat. Pulls are defined to test the correct determination of the covariance matrix and are a measure of the displacement of the reconstructed values to the fitted values. They are constructed such that a valid distribution of pulls will form a normal distribution with a width of one and a mean of zero. Pulls are very sensitive to the goodness of the fit. If the width deviates from one, the resolution derived in the reconstruction does not reflect the true errors and it is necessary to globally scale the measured initial errors to force the pull distributions to have a width of one. No scaling factors are needed in this analysis for events with two photons in the final state. For events with six photons in the final state, scaling factors have been determined carefully for data and Monte Carlo events. Typical confidence-level and pull distributions are shown in Fig. 3. The CL values were found to be sufficiently flat in all photon-energy bins.

In a first step of kinematic fitting, a consistency check was carried out by imposing energy and momentum conservation on all events. The hypothesis,

$$\gamma p \to p n_\gamma \gamma, \tag{4}$$

was tested, where n_γ is the number of photons in the final state [i.e., two for reaction (1) and six for reactions (2) and (3)]. Energy and momentum conservation provides four equations that any event from reaction (4) must satisfy. Thus, the proton three-momentum can be left "missing" and reconstructed from other observables, still retaining one constraint (1C) provided by the photon energies and directions. Table I summarizes the hypotheses used to select events for $\gamma p \to p\eta$ and $\gamma p \to p\eta'$.

A prompt coincidence between a photon in TAPS and an electron in the tagger was required to reduce time-accidental background. Random time coincidences underneath the prompt peak (Fig. 4) were subtracted by performing the exact same selection procedure for events outside the prompt time coincidence window. Figure 5 (left) shows the invariant $\gamma\gamma$ mass (time-accidental background subtracted) for kinematically fitted two-photon events. A confidence level cut at 10^{-2} was applied. Clear peaks for the π^0 and η mesons are visible. The background underneath the peaks depends on kinematics and is on the average smaller than 4%, but can be up to 15% at high energies and in the most forward angle bins. In addition to energy and momentum conservation,

TABLE I. Kinematic fits and constraints used in the analysis. The proton is treated as missing particle. Its momentum is determined from the kinematic fit. For the η' reconstruction, only one pion mass was imposed in the kinematic fit (3C fit).

Reaction	Decay mode	Constraints	Fit
$\gamma p \to p\eta$	$\eta \to 2\gamma$	$(E, \vec{p})$ conservation	1C
$\gamma p \to p\eta$	$\eta \to 3\pi^0 \to 6\gamma$	$(E, \vec{p})$ conservation	1C
		$+ 3 \times \pi^0$ mass	4C
$\gamma p \to p\eta'$	$\eta' \to 2\pi^0\eta \to 6\gamma$	$(E, \vec{p})$ conservation	1C
		$+ \pi^0$ and η masses	3C

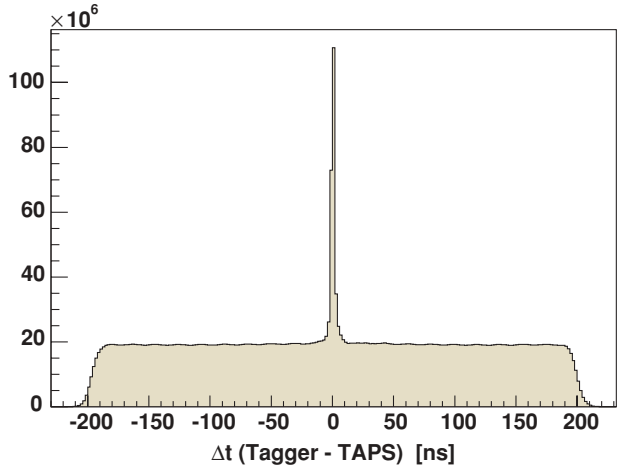

FIG. 4. (Color online) Time difference between photons in TAPS (mean value for all photons) and electrons in the tagger integrated over all events. A prompt coincidence is defined by $-3 < \Delta t < 3$ ns.

three π^0 mass constraints were imposed on events from $\gamma p \to p\eta \to p3\pi^0 \to p6\gamma$ (4C kinematic fit) reducing significantly combinatorial background. A confidence level cut at 10^{-3} was applied. The invariant $3\pi^0$ mass is shown in Fig. 5 (middle). The η peak is visible above a small combinatorial background. The uncertainty in signal lost from CL cuts in data compared to Monte Carlo is estimated to be less than 3%.

In a final step of the η analysis, mass cuts were applied in the two-photon spectrum and in the $3\pi^0$ spectrum. The width of the η peak varied as a function of incident photon energy between $\sim$12 MeV/c^2 at the lowest energies and $\sim$17 MeV/c^2 at the highest energies. The remaining background underneath the $\eta_{\gamma\gamma}$ and $\eta_{3\pi^0}$ peaks was subtracted using side bins for every $(E_\gamma, \cos\theta)$ bin.

For the selection of η' events, the hypothesis $\gamma p \to p\pi^0\eta\gamma\gamma$ was tested in addition to reaction (4) with a confidence-level cut at 10^{-2}. The remaining invariant $\gamma\gamma$ mass is shown in Fig. 6 (left). The second π^0 was reconstructed with $110 < m_{\pi^0\to\gamma\gamma} < 160$ MeV/c^2. Figure 5 (right) shows a clear peak for the η' in the invariant $2\pi^0\eta$ mass spectrum. Moreover, an interesting enhancement is visible at 1250 MeV/c^2, giving rise to a possible contribution of the controversial meson $\eta(1295)$ and/or the $f_1(1285)$. Additional studies of this signal are statistically challenging and are not discussed further here. Events from reaction (3) were finally selected with $910 < m_{2\pi^0\eta} < 1010$ MeV/c^2. The remaining background was determined in fits to the η' peaks. An alternative way of reconstructing η' events via $\gamma p \to p\pi^0\pi^0\gamma\gamma$ was used for systematic checks. The invariant $\gamma\gamma$ mass is shown in Fig. 6 (right).

B. Monte Carlo simulations

The performance of the detector was simulated in GEANT3-based Monte Carlo studies. The program package used for CBELSA/TAPS is built upon a program developed for the CB-ELSA experiment. The Monte Carlo program reproduces accurately the response of the TAPS and Crystal-Barrel crystals when hit by a photon. For charged particles, the detector response is known to a lower precision but is still reasonably well understood.

The acceptance for reactions (1)–(3) was determined by simulating events, which were evenly distributed over the available phase space. The Monte Carlo events were analyzed using the same reconstruction criteria, which were also applied to the (real) measured data. The same hypotheses were tested in the kinematic fits and events selected with the same confidence level cuts. The acceptance is defined as the ratio of the number of generated to reconstructed Monte Carlo events,

$$A_{\gamma p\to pX} = \frac{N_{\mathrm{rec,MC}}}{N_{\mathrm{gen,MC}}} \qquad (X = \eta, \eta'). \tag{5}$$

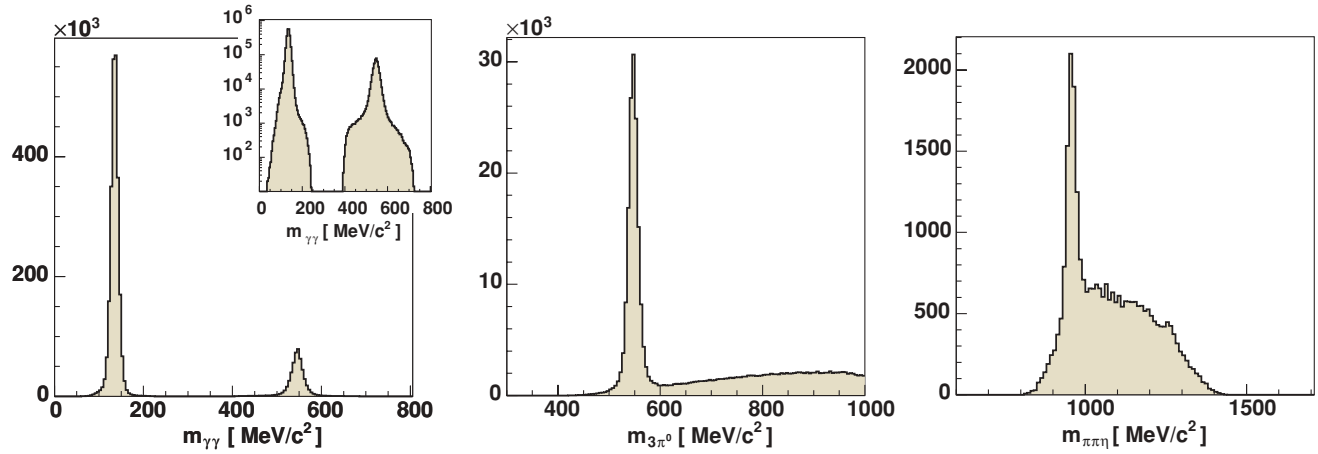

FIG. 5. (Color online) Invariant mass spectra (integrated over all photon energies) for the reactions $\gamma p \to p\gamma\gamma$ (left) and $\gamma p \to p\pi^0\pi^0\pi^0$ (center); confidence-level cuts were applied at 10^{-2} and at 10^{-3}, respectively. In the two-photon decay mode, the π^0 and η mesons are observed with very little background. The inset on the left shows the distribution using a logarithmic scale; the gap between 200 and 400 MeV/c^2 stems from a loose kinematic cut before kinematic fitting requiring the proton and the two-photon system to go back-to-back in the center-of-mass system. The invariant $\pi^0\pi^0\eta$ mass spectrum (right) shows a clear η' signal and an enhancement at 1250 MeV/c^2.

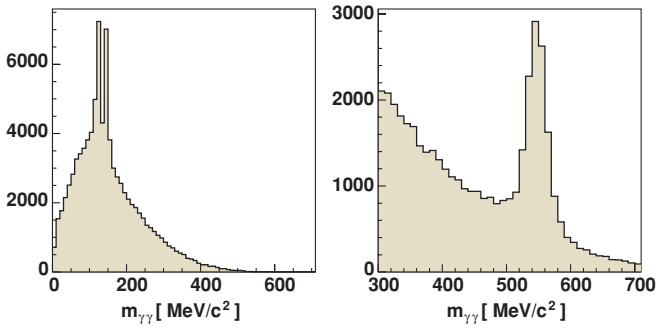

FIG. 6. (Color online) Invariant $\gamma\gamma$ mass spectra (integrated over all incoming photon energies) for the two reactions $\gamma p \to p\pi^0\eta\gamma\gamma$ (left) and $\gamma p \to p\pi^0\pi^0\gamma\gamma$ (right). The π^0 signal shows a double-peak structure because the "better" π^0 was found in the kinematic fit.

The trigger required either two hits above a low-energy threshold in TAPS (LED low) or one hit above a higher-energy threshold in TAPS (LED high) in combination with at least one cluster in the Crystal-Barrel calorimeter. The second-level trigger used a fast cluster encoder based on a cellular logic to define the number of contiguous Crystal-Barrel clusters. The decision time depended on the complexity of the hit distribution in the Crystal-Barrel and was typically 4 μs. In case of an event rejection, a fast reset was generated, which cleared the readout electronics in 5 μs. Otherwise the readout of the full event was initiated with typical readout times of 5–10 ms. To properly simulate the detector response, FACE and TAPS-LED thresholds had to be determined from the data for all crystals. Given the different response characteristics of protons and photons in BaF_2 crystals, protons experience slightly different LED thresholds than photons. For this reason, we have corrected the measured proton energy according to $0.8 \cdot E_p + 30$ MeV, which is derived from available proton times in TAPS and from Monte-Carlo studies. At the reaction threshold, when the proton is required in the (TAPS) trigger, corrections are small. Above about 1 GeV in the incoming photon energy, the proton trigger is not relevant. Our understanding of the threshold function is fair to good and reasonably well reproduced in the trigger simulation.

IV. DETERMINATION OF CROSS SECTIONS

The differential cross sections for this analysis are determined according to

$$\frac{d\sigma}{d\Omega} = \frac{N_{X\to n_\gamma\gamma}}{A_{X\to n_\gamma\gamma}} \frac{1}{N_\gamma \rho_t} \frac{1}{\Delta\Omega} \frac{1}{\frac{\Gamma_{X\to n_\gamma\gamma}}{\Gamma_{\text{total}}}}, \tag{6}$$

where ρ_t is the target area density; $N_{X\to n_\gamma\gamma}$ is the number of reconstructed data events in an $(E_\gamma, \cos\theta_{\text{c.m.}})$ bin; N_γ is the number of photons in an (E_γ) bin; $A_{X\to n_\gamma\gamma}$ is the acceptance in an $(E_\gamma, \cos\theta_{\text{c.m.}})$ bin; $\Delta\Omega$ is the solid-angle interval $\Delta\Omega = 2\pi\,\Delta\cos(\theta_{\text{c.m.}})$; and $\frac{\Gamma_{X\to n_\gamma\gamma}}{\Gamma_{\text{total}}}$ is the decay branching fraction.

The target area density, i.e., the number of atoms in the target material per cross-sectional area (orthogonal to the photon beam), is given by

$$\rho_t = 2\frac{\rho(H_2) N_A L}{M_{\text{mol}}(H_2)} = 2.231 \times 10^{-7}\,\mu\text{b}^{-1}, \tag{7}$$

where $\rho(H_2) = 0.0708$ g/cm^3 is the density and $M_{\text{mol}} = 2.01588$ g/mol is the molar mass of liquid H_2. $N_A = 6.022 \times 10^{23}$ mol^{-1} is the Avogadro number and $L = 5.275$ cm is the length of the target cell. The factor of two accounts for the molecular composition of hydrogen (H_2).

The cross sections were extracted independently for both η decay modes, $\eta \to \gamma\gamma$ as well as $\eta \to 3\pi^0$, and then averaged (weighted with their errors) based on the observed good agreement (see Fig. 7 and Sec. V A). The number of events in an $(E_\gamma, \cos\theta_{\text{c.m.}})$ bin comprises events with two or three final-state particles (at least 2γ's) or six or seven "particles" (at least 6γ's), respectively. The proton can be "missing," but events with and without the detected proton are treated in the same way in the event reconstruction. At threshold, the event kinematics requires that the proton is used in the (TAPS) trigger. Thus, the threshold function for the detection of low-energy protons needs to be reasonably well understood.

The interval of the solid angle is given by $\Delta\Omega = 2\pi\,\Delta\cos(\theta_{\text{c.m.}})$ with $\Delta\cos(\theta_{\text{c.m.}})$ describing the width of the angular bins. It was chosen to be 0.1 for the η data presented here. Energy bins were defined by considering statistics and ensuring a good comparability with other experiments. A total of 34 bins is presented in energy steps of 50 MeV for $E_\gamma \in [850, 2550]$ MeV. For the η' data, $\Delta\cos(\theta_{\text{c.m.}})$ was chosen to be 0.2. A total of 20 bins is presented in energy steps of 50 MeV for $E_\gamma \in [1500, 2550]$ MeV.

The number of observed η and η' mesons needs to be corrected for unseen decay modes. Partial-decay branching fractions used to correct the measured cross sections are taken from Ref. [15]: $\text{BR}(\eta \to 2\gamma) = 0.3931 \pm 0.002$, $\text{BR}(\eta \to 3\pi^0 \to 6\gamma) = 0.3256 \pm 0.0023$, and $\text{BR}(\eta' \to 2\pi^0\eta \to 6\gamma) = 0.207 \pm 0.012$.

A. Normalization

The tagging hodoscope consisted of 480 scintillating fibers above 14 partially overlapping scintillation counters (tagger bars). The photon flux was measured directly in the experiment and determined according to

$$N_\gamma = N_{\text{scaler}}^{\text{fiber}} \cdot \alpha \cdot P_\gamma, \tag{8}$$

where $N_{\text{scaler}}^{\text{fiber}}$ are the free hardware counts for the individual fibers corrected for the lifetime of the detector. The parameter α accounts for the (fiber)-cluster reconstruction in the tagger, which has to be performed in the same way as for real hadronic events. The photon definition probability, or P_γ, denotes the probability that a real photon is emitted along the beam axis in the tagger and traverses the liquid hydrogen target. The scalers are recorded in scaler events, which were accumulated with a minimum-bias trigger at a rate of 1Hz during the regular data taking. This trigger required only a hit in the tagger and was thus independent of hadronic cross sections. The parameter P_γ is determined from Tagger-Or-Runs—separate data runs utilizing a minimum-bias trigger.

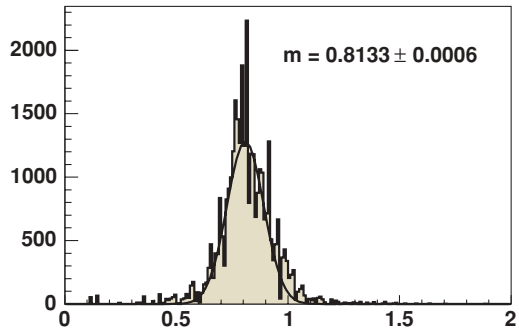

FIG. 7. (Color online) Ratio $\Gamma_{\eta\to 3\pi^0}/\Gamma_{\eta\to 2\gamma}$ for each $(E_\gamma, \cos\theta_{\text{c.m.}})$ bin. The values are weighted with their squared inverse errors.

The total error of the photon flux is assumed to be dominated by the P_γ error and depends strongly on the efficiency of the beam monitor at the end of the beam line (Fig. 1). P_γ was determined to $0.639 \pm 0.002_{\text{stat.}} \pm 0.05_{\text{sys.}}$ by varying the background subtraction of noncoincident tagger-beam monitor hits. This value is consistent with determinations from multiple Tagger-Or-Runs at different incoming photon rates. An overall error of 10% has been assigned to the photon flux determination. This error is included in the error band (see Figs. 9 and 10).

B. Systematic uncertainties

The statistical errors are determined from the number of events in each $(E_\gamma, \cos\theta_{\text{c.m.}})$ bin. Statistical errors are shown for all data points; systematic uncertainties are given as error bands at the bottom of each plot.

The systematic errors include uncertainties from the position of the liquid hydrogen target and a possible offset of the photon beam. The position of the target cell was determined from kinematic fitting by comparing the off-zero displacement of different pull distributions to Monte Carlo simulations. It was found to be shifted upstream by 0.65 cm [38]. The corresponding systematic errors were determined by varying the target position in the Monte Carlo (± 1.5 mm) and evaluating changes in the re-extracted differential cross sections. The errors show an angular dependence, but are 2%−3% on the average and $\leqslant 5\%$ at most around $\cos\theta_{\text{c.m.}} = 0$. The photon beam was assumed to be shifted by <2 mm off axis at the target position. The errors of the decay branching fractions are negligible. The uncertainty of the proton trigger has been determined from the small disagreement of the differential η cross sections using the $\eta \to 2\gamma$ and $\eta \to 3\pi^0 \to 6\gamma$ decay channels for $E_\gamma < 1$ GeV and $\cos\theta_{\text{c.m.}} < 0.0$ (Fig. 8).

The reconstruction of neutral mesons and the identification of final states require a sequence of cuts including the use of kinematic fitting. As discussed in the following section, the reconstruction of η mesons from final states with two and six photons leads to compatible results. This fact emphasizes a good understanding of the detector response to multiphoton final states. An overall $\pm 5.7\%$ error is assigned to the reconstruction efficiency as determined in Ref. [39]. An additional 3% systematic error accounts for the slightly different effects

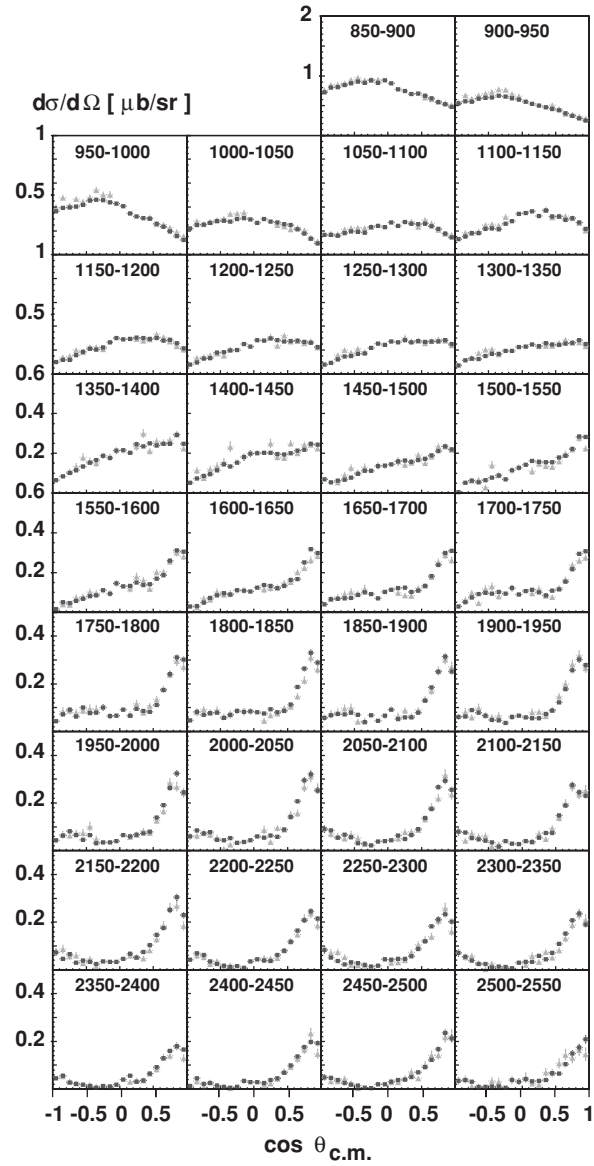

FIG. 8. Differential cross sections for $\gamma p \to p\eta$ using the $\eta \to 2\gamma$ (■) and $\eta \to 3\pi^0 \to 6\gamma$ (▲) decay channels. Only statistical errors are assigned to the data points. In some bins, the acceptance for $\eta \to 3\pi^0$ is small (<5%) and, thus, corresponding data points are not shown. The figure shows the excellent agreement of both reactions.

of confidence-level cuts on data and Monte Carlo events. All these errors are added quadratically to give the total systematic error. Moreover, the η' systematic error receives an additional contribution from an alternative way of reconstructing events via $\gamma p \to p\pi^0\pi^0\gamma\gamma$ (Sec. III A).

V. EXPERIMENTAL RESULTS

A. Differential cross sections $d\sigma/d\Omega$ for $\gamma p \to p\eta$ at an electron-beam energy of $E_{e^-} = 3.18$ GeV

Figure 8 shows the $\gamma p \to p\eta$ differential cross sections for the two different η decay modes (1) and (2). We have excluded

those data points in the analysis showing a Monte Carlo acceptance of <5%. The data sets show excellent agreement.

We have checked the consistency of the two cross-section measurements by forming the ratio of partial widths of the two η decay modes. Because the cross sections in Fig. 8 are corrected for the decay branching ratios, we determine

$$\frac{\Gamma_{\eta\to 3\pi^0}}{\Gamma_{\eta\to 2\gamma}} = \frac{\left[\frac{d\sigma}{d\Omega}(E_\gamma, \cos\theta_{\text{c.m.}})\right]_{\eta\to 3\pi^0}\left[\frac{\Gamma_{\eta\to 3\pi^0}}{\Gamma_{\text{total}}}\right]_{\text{PDG}}}{\left[\frac{d\sigma}{d\Omega}(E_\gamma, \cos\theta_{\text{c.m.}})\right]_{\eta\to 2\gamma}\left[\frac{\Gamma_{\eta\to 2\gamma}}{\Gamma_{\text{total}}}\right]_{\text{PDG}}}, \qquad (9)$$

for each (E_γ,cos $\theta_{\text{c.m.}}$) bin. The values are weighted with their squared inverse errors and histogrammed (Fig. 7). We derive a peak position of

$$\frac{\Gamma_{\eta\to 3\pi^0}}{\Gamma_{\eta\to 2\gamma}} = (0.8133 \pm 0.0006_{\text{stat.}} \pm 0.0138_{\text{sys.}}), \qquad (10)$$

where the systematic error is derived from considering all systematic uncertainties discussed in Sec. IV B. We do not claim a new measurement of η branching fractions here, but have rather used this number to check our reconstruction efficiency. The Particle Data Group gives two values for this branching ratio [15]: (0.829 ± 0.007) is the mean value of all direct measurements whereas a combined fit to all partial decay widths yields a value of (0.828 ± 0.006). Both PDG values are consistent with our result.

B. Differential cross sections $d\sigma/d\Omega$ for $\gamma p \to p\eta$—combined data set

Because the differential cross sections for the two η decay modes are consistent, we have calculated error-weighted mean values. These are presented in Fig. 9 as functions of energy and the η production angle. Because the cross sections change rather smoothly, only few resonances are likely to contribute to the process. The $N(1535)S_{11}$ state is known to dominate the threshold region resulting in a flat distribution in cos $\theta_{\text{c.m.}}$; interference with other amplitudes leads to deviations from that flat distribution. At higher energies, above $E_\gamma = 1.5$ GeV, the development of a forward peak indicates important contributions from t-channel ρ and ω exchange.

Figure 9 also shows a comparison of our new η results to published results from CB-ELSA [8]. The agreement between the two data sets is very good at lower energies. However, the differential cross sections reported by CB-ELSA show somewhat larger discrepancies at higher energies and forward angles. Above $E_\gamma = 2.5$ GeV and in the forward-most angle bins, CB-ELSA results are approximately 30% larger than our new CBELSA/TAPS results at these energies, but are still consistent within the errors. We believe that the discrepancy is from underestimated background in the CB-ELSA data in the low-statistics forward-most bins where fewer than ten events were observed.

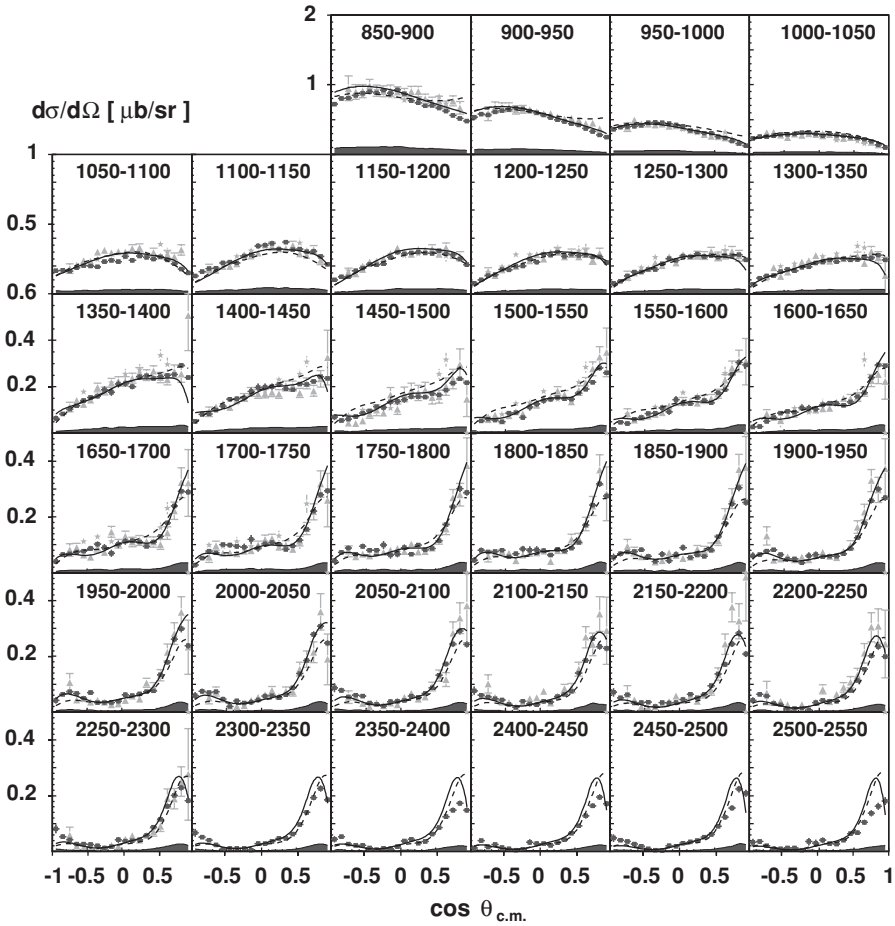

FIG. 9. Differential cross sections for $\gamma p \to p\eta$ (■) using the combined data set of $\eta \to 2\gamma$ and $\eta \to 3\pi^0 \to 6\gamma$ events. For comparison, CB-ELSA data [8] are represented by (▲) and CLAS data by (★). The solid line shows our previous PWA solution [8] and the dashed line represents the SAID model [40]. The data points include statistical errors only; the total systematic error is given as error bands at the bottom of each plot.

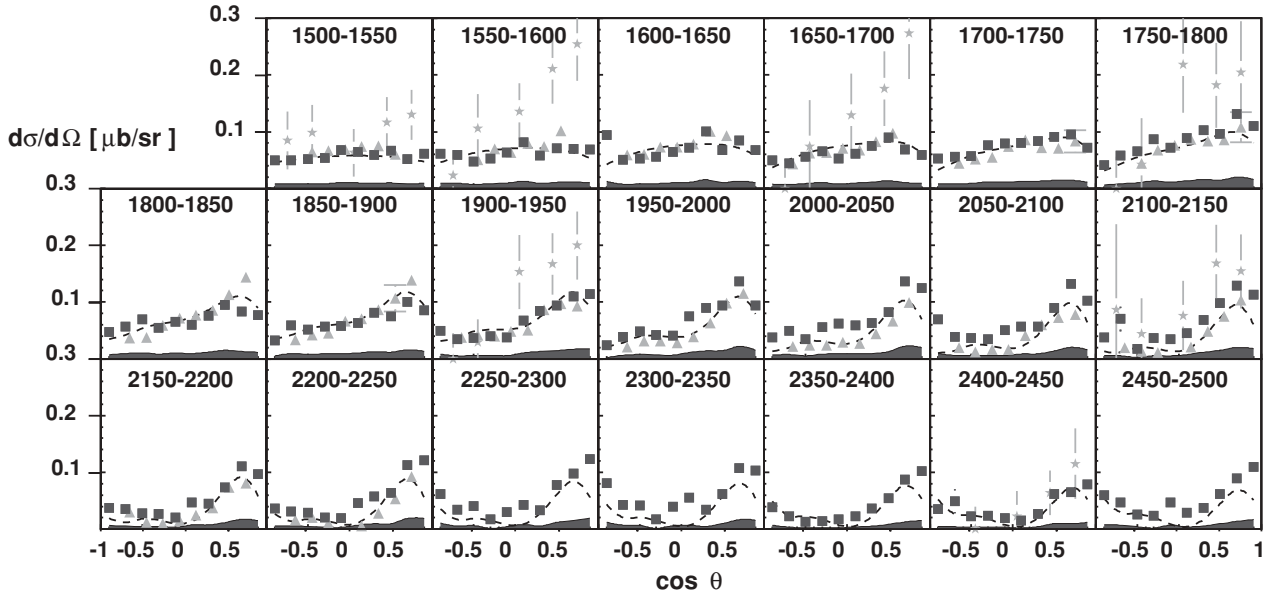

FIG. 10. Differential cross sections for the reaction $\gamma p \to p\eta'$ (analyzed decay mode $\eta' \to 2\pi^0\eta \to p6\gamma$) (■) using 50-MeV-wide energy bins and cos $\theta^{\eta'}_{\text{c.m.}}$ bins of width 0.2. The data cover the full angular range; energies are given in MeV. For comparison, data are shown from SAPHIR [28] (★) and CLAS [29] (▲). The SAPHIR data are based on only 250 events and, thus, have large error bars. The dashed line represents the SAID model [40].

C. Differential cross sections $d\sigma/d\Omega$ for $\gamma p \to p\eta'$ at an electron-beam energy of $E_{e^-} = 3.18$ GeV

Figure 10 shows the differential cross sections for the reaction $\gamma p \to p\eta' \to 2\pi^0\eta$ [reaction (3)] using cos $\theta^{\eta'}_{\text{c.m.}}$ bins of width 0.2. The data cover the full angular range. Very similar to η photoproduction, a rather flat angular distribution is observed at low energies suggesting s-channel resonance production near threshold. Both data sets also show a continuing increase in slope at forward angles, which becomes more prominent at higher energies. This forward peak is most likely from t-channel exchange mechanisms. Moreover, our new data indicate a decrease in the forward-most bin, which has not been observed before. Above 2 GeV in photon energy, growth at backward angles could be indicative of u-channel contributions. The overall agreement between the CBELSA/TAPS and CLAS data is good at threshold to fair above $E_\gamma = 1800$ MeV.

The s-wave behavior of the reaction close to the reaction threshold is apparent from the experimental data. Figure 11 shows the differential cross sections for $\gamma p \to p\eta'$ at and close to the reaction threshold using 5 cos $\theta^{\eta'}_{\text{c.m.}}$ bins of width 0.4. The cross sections have been determined for individual fibers of the tagging system and cover the full angular range. The data points suffer from low statistics, but are overall consistent with

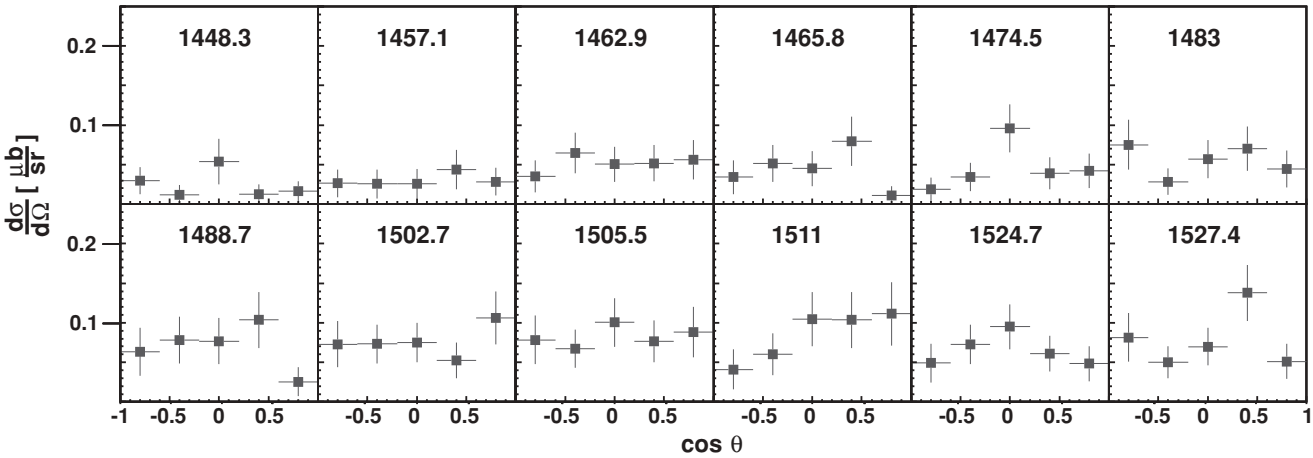

FIG. 11. Differential cross sections for the reaction $\gamma p \to p\eta'$ close to the reaction threshold (■) determined for individual tagger channels using 5 cos $\theta^{\eta'}_{\text{c.m.}}$ bins of width 0.4. Energies in the plots are given in MeV. Although limited in statistics, all angular distributions appear to be flat indicating s-wave behavior of the reaction at the threshold.

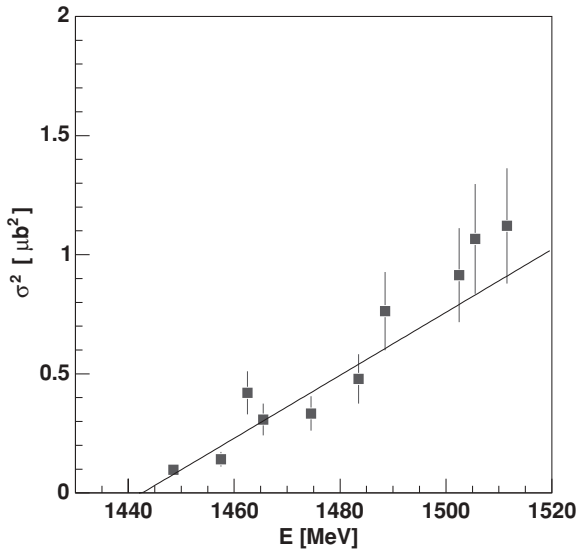

FIG. 12. Shown is the linear energy dependence of the squared total cross section, $\sigma^2_{\rm tot}$, for the reaction $\gamma p \to p\eta'$ close to the reaction threshold of $E_{\rm thres} \approx 1447$ MeV.

flat angular distributions. The expected energy dependence of the reaction at the threshold is given by [41]

$$\sigma(E_\gamma) \propto (E_\gamma - E_{\rm thres})^{l+1/2} \qquad l = 0, 1, 2, \ldots, \qquad (11)$$

where l denotes s, p, d ... waves, etc. For s-wave dominance, a linear energy dependence of the squared total cross section is, thus, expected close to the reaction threshold. The differential cross sections shown in Fig. 11 have been used to determine the total η' cross section and to study the energy dependence. Because the data cover the full angular range, no extrapolation is needed. Figure 12 shows the incoming photon energy plotted versus the squared total cross section. A linear dependence is clearly observed and a fit determines the energy threshold to (1442.6 ± 3.8) MeV, which is compatible with the value of (1446.38 ± 0.48) MeV derived from the η' mass listed in the PDG [15]. The mass of the η meson was determined by the TAPS/A2 Collaboration in a very similar procedure [1,42].

D. The total cross sections

Figure 13 shows the total cross section for η photoproduction. Because of the complete solid angle coverage, no extrapolation is required and the data points are truly experimental. In the low-energy range, the S_{11} partial wave dominates the cross section. The solid line represents our previous PWA solution and is not a fit to these data; the two states $N(1720)P_{13}$ and $N(2070)D_{15}$ saturated the total cross section [8]. A new PWA solution, including the new CBELSA/TAPS data presented here and other data sets, is in preparation. It is clear that single- and double-polarization variables are required to firmly establish resonance contributions. Coupled channel fits to many reactions can also help; in particular, when three-body final states are included, the phase of two-particle partial-wave amplitudes is tested in the crossed channel.

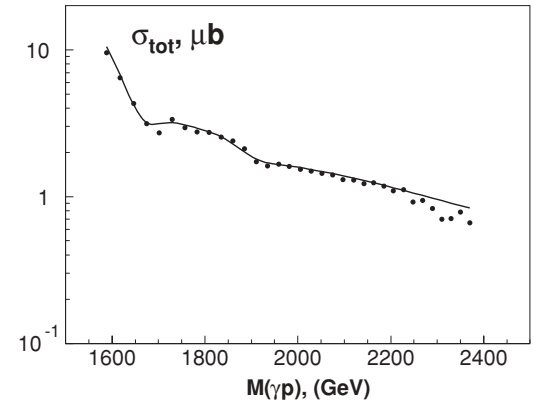

FIG. 13. Total $\gamma p \to p\eta$ cross section. The data points (•) are calculated by summation of the differential cross section; the gray line represents the result of our previous partial wave analysis.

A small anomaly is observed at 1.73 GeV/c^2 in the total η cross section. As discussed earlier, recent data off the neutron show a pronounced bumplike structure at 1.68 GeV [22], which has been suggested to signal the existence of a narrow baryon state with $(M \approx 1.68, \Gamma \leqslant 30)$ MeV/c^2. In particular, the possibility that this state could be the $N(1650)P_{11}$, nonstrange member of an antidecuplet of pentaquarks is certainly interesting [43–45]. Figure 14 shows the total number of $\eta \to \gamma\gamma$ events for the tagger channels 419–431. The data have been fitted using a polynomial to indicate the smooth behavior of the distribution. The data point at 1.73 GeV/c^2 in the total cross section is based on the photon energy interval $E_\gamma \in [1100, 1150]$ MeV defined by the tagger channels $E_\gamma \in [421, 426]$. No statistically significant enhancement is observed in Fig. 14 over the small energy range under investigation to explain the anomaly, and a narrow state compatible with the observation in the total cross section can be

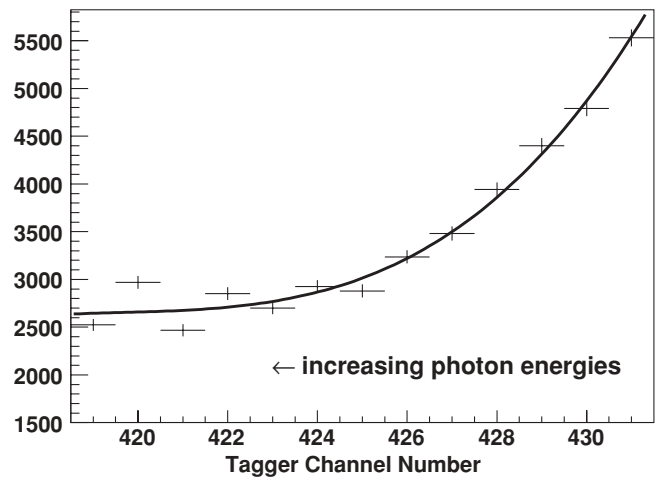

FIG. 14. Total $\eta \to \gamma\gamma$ yields per tagger channel number covering the energy range of the anomaly observed in the total η cross section. The data point at 1.73 GeV/c^2 (see Fig. 13) is based on channels 421–426. No statistically significant enhancement can be seen in the excitation function.

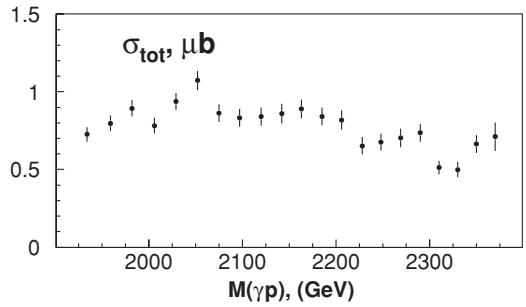

FIG. 15. Total $\gamma p \to p\eta'$ cross section. The data points (•) are calculated by summation of the differential cross section.

ruled out. We believe that this structure is an instrumental effect originating from tagger cluster-size corrections of low-rate Tagger-Or-Data used in the photon-flux determination, which occurs only for those channels.

In Fig. 15, the total cross section for η' photoproduction is displayed. Again, because of the complete solid angle coverage, no extrapolation is required. At 2 GeV in the invariant mass and above, the cross section for η' production is about 50% of that for η production assuming that the processes are dominated by ρ, ω-exchange resonances. For a pseudoscalar mixing angle of $\Theta_{PS} = -19.3^\circ$, the non-$s\bar{s}$ components of η' and η differ by a factor of 1/2. The similarity of the two numbers suggests that the dynamics of η and η' photoproduction is similar.

VI. RECENT RESULTS OF THE BONN-GATCHINA MODEL

The analysis of previous CB-ELSA data on photoproduction of η mesons [8,12] revealed two surprises. (1) The analysis suggested a new resonance with spin and parity $J^P = 5/2^-$, $N(2070)D_{15}$ [24]. The total cross section was nearly saturated with three resonances, the well-known $N(1535)S_{11}$, the $N(1720)P_{13}$, and the new resonance. (2) The strong coupling of $N(1720)P_{13} \to N\eta$ was also unexpected; in MAID [25,46], the $N(1710)P_{11} \to N\eta$ was very significant whereas $N(1720)P_{13}$ hardly contributed to η photoproduction.

The pattern of states contributing most to η photoproduction, $N(1535)S_{11}$, $N(1720)P_{13}$, $N(2070)D_{15}$, was interpreted as a sequence of quark model states with total intrinsic angular momenta $L = 1, 2, 3$ and $S = 1/2$ coupling to $J^P = 1/2^-, 3/2^-, 5/2^-$. The regularity of this pattern was used to argue that the seed of $N(1535)S_{11}$ should be of a three-quark nature; because of the presence of S-wave thresholds, the state may attract large $N\eta$ and $\Sigma\pi$ molecular components.

The relative strength of the two nucleon excitations at an incoming photon energy of 1700 MeV in $\gamma p \to p\eta$ remains disputed. The Gießen group [47] found—like MAID—$N(1710)P_{11} \to N\eta$ to provide a significant contribution. Other coupled channel analyses confirmed the dominance of $N(1720)P_{13}$ [relative to $N(1710)P_{11}$]. In Refs. [48] and [49], a large variety of η production data was fitted using an effective Lagrangian approach; in both analyses, the $N(1720)P_{13}$ contribution was considerably larger than that of $N(1710)P_{11}$. A chiral quark model approach complemented with a one-gluon exchange model [50] arrived at the same conclusion.

Restricted to photoproduction data, the best solution for the new data presented here (in terms of its χ^2 value) still supports the dominance of the three nucleon resonances, $N(1535)S_{11}$, $N(1720)P_{13}$, and $N(2070)D_{15}$ in η photoproduction. However, this solution is incompatible with data on $\pi^- p \to n\eta$. This is presently being investigated further and will be the subject of a forthcoming publication of the Bonn-Gatchina partial wave analysis group.

VII. SUMMARY

In summary, we have presented data on the photoproduced η and η' cross sections from the reactions $\gamma p \to p\eta$ with $\eta \to 3\pi^0 \to 6\gamma$ as well as $\eta \to 2\gamma$ and from the reaction $\gamma p \to p\eta'$ with $\eta' \to \pi^0\pi^0\eta \to 6\gamma$. The continuous beam from the ELSA accelerator and the fiber detector of the tagging system provided tagged photons in the energy range from 850 to 2550 MeV. The results are in very good agreement with previous measurements, but extend over the full angular range in $\cos\theta_{c.m.}$ of the η and η' meson. The inclusion of the new η data into a multichannel partial wave analysis is in preparation. The threshold behavior of the η' data indicate s-wave dominance.

ACKNOWLEDGMENTS

We thank the technical staff at ELSA and at all the participating institutions for their invaluable contributions to the success of the experiment. We acknowledge financial support from the National Science Foundation (NSF), Deutsche Forschungsgemeinschaft (DFG) within the SFB/TR16, and Schweizerischer Nationalfond. Through collaboration with St. Petersburg, funds were received from DFG and the Russian Foundation for Basic Research.

[1] B. Krusche *et al.*, Phys. Rev. Lett. **74**, 3736 (1995).
[2] J. Ajaka *et al.*, Phys. Rev. Lett. **81**, 1797 (1998).
[3] A. Bock *et al.*, Phys. Rev. Lett. **81**, 534 (1998).
[4] C. S. Armstrong *et al.* (Jefferson Lab E94014 Collaboration), Phys. Rev. D **60**, 052004 (1999).
[5] R. Thompson *et al.* (CLAS Collaboration), Phys. Rev. Lett. **86**, 1702 (2001).
[6] F. Renard *et al.* (GRAAL Collaboration), Phys. Lett. **B528**, 215 (2002).
[7] M. Dugger *et al.* (CLAS Collaboration), Phys. Rev. Lett. **89**, 222002 (2002) [Erratum-*ibid.* **89**, 249904 (2002)].
[8] V. Crede *et al.* (CB-ELSA Collaboration), Phys. Rev. Lett. **94**, 012004 (2005).

[9] D. Elsner *et al.* (CBELSA/TAPS Collaboration), Eur. Phys. J. A **33**, 147 (2007).
[10] H. Denizli *et al.* (CLAS Collaboration), Phys. Rev. C **76**, 015204 (2007).
[11] M. Williams *et al.* (CLAS Collaboration), arXiv:0909.0616 [nucl-ex].
[12] O. Bartholomy *et al.* (CB-ELSA Collaboration), Eur. Phys. J. A **33**, 133 (2007).
[13] J. Denschlag, L. Tiator, and D. Drechsel, Eur. Phys. J. A **3**, 171 (1998).
[14] L. Tiator, G. Knochlein, and C. Bennhold, PiN Newslett. **14**, 70 (1998).
[15] Particle Data Group, C. Amsler *et al.*, Phys. Lett. **B667**, 1 (2008).
[16] N. Isgur and G. Karl, Phys. Lett. **B72**, 109 (1977).
[17] N. Kaiser, P. B. Siegel, and W. Weise, Phys. Lett. **B362**, 23 (1995).
[18] D. Jido, J. A. Oller, E. Oset, A. Ramos, and U.-G. Meißner, Nucl. Phys. **A725**, 181 (2003).
[19] D. Jido, M. Doring, and E. Oset, Phys. Rev. C **77**, 065207 (2008).
[20] B. Julia-Diaz, T. S. H. Lee, A. Matsuyama, T. Sato, and L. C. Smith, Phys. Rev. C **77**, 045205 (2008).
[21] V. Kuznetsov (GRAAL Collaboration), Workshop on the Physics of Excited Nucleons (NSTAR 2004), Grenoble, France, 24–27 March 2004, arXiv:hep-ex/0409032.
[22] I. Jaegle *et al.* (CBELSA/TAPS Collaboration), Phys. Rev. Lett. **100**, 252002 (2008).
[23] A. V. Anisovich, I. Jaegle, E. Klempt, B. Krusche, V. A. Nikonov, A. V. Sarantsev, and U. Thoma, Eur. Phys. J. A **41**, 13 (2009).
[24] A. V. Anisovich, A. Sarantsev, O. Bartholomy, E. Klempt, V. A. Nikonov, and U. Thoma, Eur. Phys. J. A **25**, 427 (2005).
[25] W. T. Chiang, S. N. Yang, L. Tiator, M. Vanderhaeghen, and D. Drechsel, Phys. Rev. C **68**, 045202 (2003).
[26] ABBHHM Collaboration, Phys. Rev. **175**, 1669 (1968).
[27] AHHM Collaboration, W. Struczinski *et al.*, Nucl. Phys. **B108**, 45 (1976).
[28] R. Plotzke *et al.* (SAPHIR Collaboration), Phys. Lett. **B444**, 555 (1998).
[29] M. Dugger *et al.*, Phys. Rev. Lett. **96**, 062001 (2006) [Erratum-*ibid.* **96**, 169905 (2006)].
[30] W. Hillert, Eur. Phys. J. A **28**, S1, 139 (2006).
[31] E. Aker *et al.*, Nucl. Instrum. Methods Phys. Res. A **321**, 69 (1992).
[32] A. R. Gabler *et al.*, Nucl. Instrum. Methods Phys. Res. A **346**, 168 (1994).
[33] R. Novotny (TAPS Collaboration), IEEE Trans. Nucl. Sci. **38**, 379 (1991).
[34] Frank Klein, Ph.D. thesis, University of Bonn (in preparation); Igor Horn, Ph.D. thesis, University of Bonn, 2004.
[35] G. Suft *et al.*, Nucl. Instrum. Methods Phys. Res. A **538**, 416 (2005).
[36] R. Castelijns *et al.* (CBELSA/TAPS Collaboration), Eur. Phys. J. A **35**, 39 (2008).
[37] M. Nanova *et al.* (CBELSA/TAPS Collaboration), Eur. Phys. J. A **35**, 333 (2008).
[38] H. van Pee *et al.* (CB-ELSA Collaboration), Eur. Phys. J. A **31**, 61 (2007).
[39] C. Amsler *et al.* (Crystal Barrel Collaboration), Z. Phys. C **58**, 175 (1993).
[40] R. A. Arndt, W. J. Briscoe, I. I. Strakovsky, and R. L. Workman, Phys. Rev. C **66**, 055213 (2002).
[41] B. Krusche and S. Schadmand, Prog. Part. Nucl. Phys. **51**, 399 (2003).
[42] B. Krusche *et al.*, Z. Phys. A **351**, 237 (1995).
[43] D. Diakonov, V. Petrov, and M. V. Polyakov, Z. Phys. A **359**, 305 (1997).
[44] M. V. Polyakov and A. Rathke, Eur. Phys. J. A **18**, 691 (2003).
[45] D. Diakonov and V. Petrov, Phys. Rev. D **69**, 094011 (2004).
[46] L. Tiator, Int. J. Mod. Phys. A **22**, 297 (2007).
[47] V. Shklyar, H. Lenske, and U. Mosel, Phys. Lett. **B650**, 172 (2007).
[48] R. Shyam and O. Scholten, Phys. Rev. C **78**, 065201 (2008).
[49] K. Nakayama, Y. Oh, and H. Haberzettl, arXiv:0803.3169 [hep-ph].
[50] J. He, B. Saghai, and Z. Li, Phys. Rev. C **78**, 035204 (2008).